CHAPTER 2

THEORY AND LITERATURE REVIEWS

THERMOELECTRIC EFFECT

The thermoelectric phenomena is comprised of three reversible effects, Seebeck, Peltier and Thomson. Moreover, three effect has been relationship with function of thermoelectric device and performance of materials are estimated by Dimensionless Figure of Merit (ZT). Then the thermoelectric device were discussed on mechanism and efficiency.
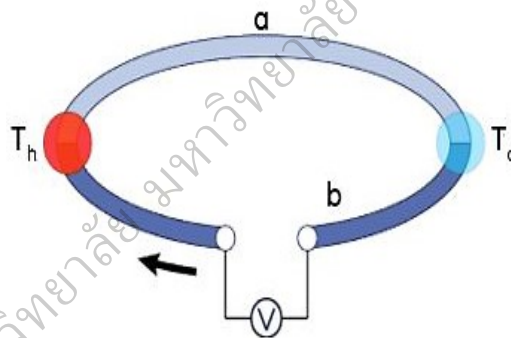
Seebeck effect

Figure 4 Schematic illustration of Seebeck effect between two dissimilar materials with junctions held at different temperatures where $T_h > T_c$. Arrow indicates the direction of current flow

In 1821 John Seebeck discovered a phenomenon that became the basis of thermoelectricity. He observed that when two dissimilar, homogeneous, conductive materials are put in a direct contact with each other creating a closed loop, an electric current will flow given the two junctions are kept at different temperatures as illustrated in Fig. 4. The temperature difference causes a more frequent generation of electron–hole pairs at higher temperatures, raising a potential gradient in the loop. As

material tries to equilibrate the charge. The temperature difference causes a more frequent generation of electron-hole pairs at higher temperatures, raising a potential gradient in the loop. As material tries to equilibrate the charge carrier surplus on the hot side, a carrier diffusion through the material towards the cold side takes place leading to an electrical diffusion current. As a result, in a n-type material, where the charge carriers are electrons, negative charges will build up at the cold side while in a p-type materials, holes will be accumulated. This effect is called the Seebeck effect and it is the direct conversion of temperature difference into electricity. (Pollock, 1985)

$$\int_{V_c}^{V_h} dV = \int_{T_c}^{T_h} S dT \tag{2.1}$$

where T_c and T_h are respectively temperature at the cold and hot end and S is the Seebeck coefficient which then can be expressed as: (Rowe, 2006)

$$S = \frac{\Delta V}{\Delta T} \tag{2.2}$$

where ΔT is the temperature difference between T_h and T_c. This implies that the produced voltage is proportional to the temperature difference, and that theoretically, the larger the temperature difference the more current flows through the loop. By convention, S, also called the thermopower, is negative for n-type and positive for p-type materials.
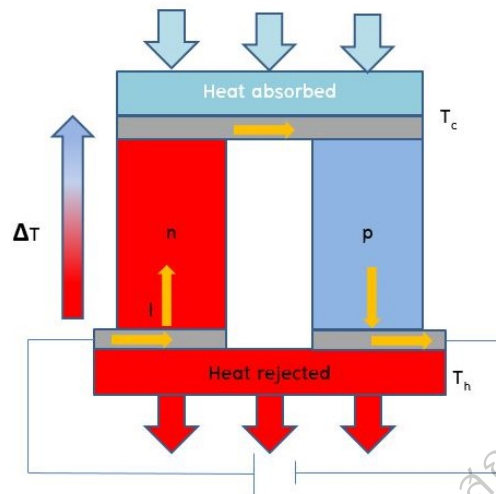
Peltier effect

Figure 5 Schematic illustration of Peltier effect in a thermocouple. The electron current flow in p and n materials which generate the heat current flow. The T_h and T_c are the temperature of hot end and cold end, respectively

When the process of power generation is reversed by applying current to a couple of two contacts materials, a temperature increase or decrease at the junction is observed. This effect was discovered by J.C Peltier in 1834 and it is illustrated in Fig. 5.

Heat release or absorption, Q, is dependent on the direction and proportional to the electric current, I, flowing through the junction, as expressed in Eq. 2.3, where $\prod$ is the Peltier coefficient. This coefficient is defined as $\frac{I}{Q}$ i.e the heat transferred reversibly with the electric current at constant temperature and it tells how much heat is carried per unit charge through the material.

$$Q = (\Pi_A - \Pi_B) \cdot I = \Pi_{AB} \cdot I \qquad (2.3)$$

$$\Pi_{AB} = S_{AB}T \qquad (2.4)$$

Thomson effect

The last thermoelectric phenomenon, the Thomson effect, describes changes in energy of a charge carriers exposed to a temperature gradient. Heat transfer is determined by the direction of the charge carrier flow meaning if a charge carrier is moving with the temperature flux it will lose energy and when it moves against the flux it will gain energy. This means that an electron will gain energy with increasing temperature and loose it when temperature decreases. The heat absorbed or liberated can be expressed as: (Loland, 2014)

$$Q = \beta I \frac{dT}{dx} \qquad (2.5)$$

where β is the Thomson coefficient, I is the electric current and $\frac{dT}{dx}$ is the temperature gradient.

The kelvin relationships

Aforementioned effects, Seebeck, Peltier and Thomson, are closely connected. This connection was proved and described by W. Thomson in 1851 in what later became known as Kelvin relationships: (Rowe, 2006)

$$S_{AB} = \frac{\Pi_{AB}}{T} \qquad (2.6)$$

$$\frac{dS_{AB}}{dT} = \frac{\beta_A - \beta_B}{T} \qquad (2.7)$$

These relationships can be derived using irreversible thermodynamics. Their validity has been demonstrated for many thermoelectric materials and it is assumed that they hold for all materials used in thermoelectric applications.

DIMENSIONLESS FIGURE OF MERIT AND THERMOELECTRIC PARAMETERS

The dimensionless figure of merit presented in Eq.2.7 describes the relationship between the three quantities determining the TE proprieties of a material: (Ohtaki, 2011, pp. 770–775)

$$ZT = \frac{\sigma S^2 T}{\kappa} = \frac{S^2 T}{\rho \kappa} \qquad (2.8)$$

where s is the Seebeck coefficient, σ is the electrical conductivity, κ is the total thermal conductivity, ρ is the electrical resistivity and T is the absolute temperature. In principle z is the thermoelectric figure of merit a material, however since it is temperature dependent it is more meaningful to use it in its dimensionless form ZT.

The thermoelectric figure of merit of a material is determined by measuring the Seebeck coefficient under small temperature gradient of 5 to 10K, the electrical conductivity under isothermal conditions, and the thermal conductivity under ≈ 1K temperature gradient. This means that the Eq. 2.8 is valid only for small temperature gradients, i.e. ΔT < 10 K (Bocher, 2009). For larger temperature gradients, the ZT value decreases with increasing ΔT mainly due to the Thomson effect which has to be then taken into consideration when designing TE devices (Min, Rowe, & Kontostavlakis, 2004, p. 1301). The ultimate goal is to have as high ZT as possible which implies that a good TE should possess (i) large Seebeck coefficient, in order to efficiently convert heat into electricity, (ii) high electrical conductivity to minimize ohmic losses and Joule heating due to electrical resistance and (iii) low thermal conductivity to minimize heat losses and maintain the thermal gradient (Molinari, Tompsett, Parker, Azough & Freer, 2014, pp. 14109–14117). The three thermoelectric parameters are functions of the carrier concentration and they are interrelated in a conflicting manner. Those relationships will be studied further in next section.

Seebeck coefficient

In an earlier section Seebeck coefficient was defined as relation between the induced voltage and the temperature difference, Eq. 2.2. By utilizing thermodynamics of irreversible processes, Seebeck coefficient can be expressed as: (Alam, H., & Ramakrishna, 2013, pp. 190–212)

$$S = \frac{8\pi^2 k_B^2}{3eh^2} m^* T (\frac{\pi}{3n})^{3/2} \tag{2.9}$$

where k_B is the Boltzman constant, e is electron charge, h is Planck's constant, m^* is the effective carrier mass, T is the absolute temperature and n is charge carrier concentration. Assuming that s is measured at constant temperature, the only variable in this equation will be carrier concentration n that can be varied through doping. By looking at the equation we can see that s will decrease when n increases. Reason for this is the fact that Seebeck effect is caused by the induced voltage in the material. The higher the carrier concentration to begin with the lower the induced voltage as it takes less new electron–hole pairs to induce current flow through the material.

Electrical conductivity

Electrical conductivity is obviously strongly affected by the carrier concentration. It is derived from the Ohmlaw and expressed as (Alam et al, 2013):

$$\sigma = \frac{1}{\rho} = ne\mu \tag{2.10}$$

where μ in this case is the carrier mobility, n is the carrier concentration and e is the electron charge.

This equation illustrates very well that σ increases with increasing carrier concentration simultaneously decreasing the electrical resistivity of the material.

In addition, electrical conductivity can be expressed through the Arrhenius equation: (Kabir et al., 2014, pp. 7522–7528)

$$\sigma = \frac{A}{T}\exp(\frac{-E_a}{k_B T}) \tag{2.11}$$

where A is the pre-exponential factor, k_B is Boltzmann's constant, T the absolute temperature and E_a the activation energy of conduction.

Thermal conductivity

In a crystalline solid, heat can be carried through the motion of charge carriers described as the electronic thermal conductivity, κ_e and through the lattice vibrations, i.e. lattice thermal conductivity, κ_l. As a result, the total thermal conductivity, κ is defined as a sum of the electronic and lattice component, Fig. 6.

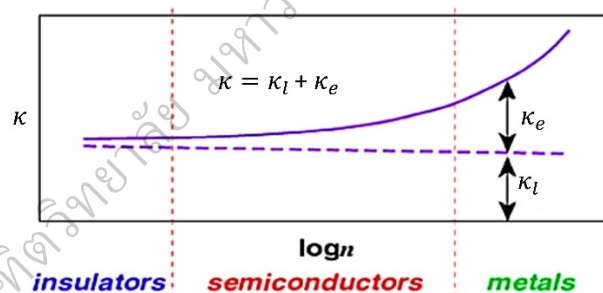$$\kappa = \kappa_l + \kappa_e \tag{2.12}$$

Figure 6 Thermal conductivity dependence on carrier concentration

(He et al., 2011)

The electronic thermal conductivity can be expressed as

$$\kappa_e = L\sigma T = \frac{LT}{\rho} \tag{2.13}$$

where L is the Lorentz number, σ is the electrical conductivity and T is the temperature. Another illustrative equation is the Wiedemann–Franz relationship (Fergus, 2012, pp. 525–540):

$$\frac{\boldsymbol{\kappa}_e}{\boldsymbol{\sigma}} = (\frac{\pi^2 k_B^2}{3e^2})T \tag{2.14}$$

where e is charge of an electron and k_B is the Boltzman's constant.

Both equations indicate that the ratio between σ and κ_e is constant at a given temperature and that any improvement in electrical conductivity leads to an offsetting increase in the electronic thermal conductivity.

The lattice thermal conductivity dominates the heat conduction process in insulators and its contribution becomes less significant the more metallic material is. Although lattice vibrations re independent of the carrier concentration the lattice thermal conductivity increases rapidly and becomes less significant in materials with high carrier concentration because the electronic thermal conductivity is the dominating process. Lattice thermal conductivity corresponds to the propagations of phonons in the three space dimensions through the crystal lattice and can be expressed as:

$$\kappa_l = \frac{1}{3}c_v v l_{ph} \tag{2.15}$$

where c_v is the heat capacity at constant volume, v is the concentration and velocity of phonons and l_{ph} is the phonon mean free path, which is defined as the average distance a phonon travels before colliding with another particle. The evolution of κ_l with the temperature depends on the dominating interactions occurring in the lattice. At low temperatures those limitations are caused by the grain size and the defect concentration while at high temperatures, collisions between phonons are the dominant factor limiting heat conduction.

ENERGY CONVERSION EFFICIENCY

In every heat engine, including the thermoelectric generator, the energy conversion efficiency is governed by the Carnot efficiency

$$\eta_c = \frac{\Delta T}{T_h} \tag{2.16}$$

The amount of electrical energy produced is dependent on the thermoelectric conversion efficiency of the device and heat flux. The conversion efficiency is a function of the temperature gradient and the thermoelectric figure of merit (ZT), defined as

$$\eta_{max} = \frac{P}{Q} = \frac{T_h - T_c}{T_h} \frac{\sqrt{1 + Z\overline{T}} - 1}{\sqrt{1 + Z\overline{T}} + \frac{T_c}{T_h}} \tag{2.17}$$

where $\overline{T} = \frac{T_h + T_c}{2}$

To maximize power generation efficiency, ZT should be as high as possible, and the temperature differential between the hot and cold sides should be as large as possible. This relation is well illustrated in Figure 7.
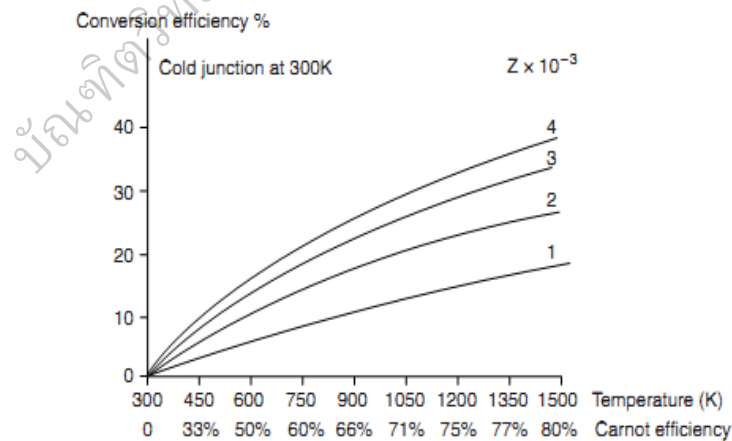

Figure 7 Generating efficiency as a function of temperature and thermoelectric material figure-of-merit (Rowe, 2006)

For practical applications Z = 1 is chosen as a benchmark as then the efficiency reaches approx. 10% (Ohtaki, Tokunaga, Eguchi, & Arai, 1997, pp. 224–227). Although it is less than more traditional technologies that can achieve 30% conversion efficiency it still is a viable addition to traditional energy production techniques. In the end the goal is not to replace existing technologies but to provide a supplement that would reduce energy losses mainly in industry where they are largest (Vining, 2009, pp. 83–85).

If it is assumed that the electrical conductivities, thermal conductivities, and Seebeck coefficients of a and b are constant within an arm, and that the contact resistances at the hot and cold junctions are negligible compared with the sum of the arm resistance, then the efficiency can be expressed as;

$$\eta = \frac{I^2 R}{S_{ab} I T_h + \kappa'(T_h - T_c) - \frac{1}{2} I^2 R} \tag{2.17}$$

where κ' is the thermal conductance of a and b in parallel and R is the series resistance of a and b. In thermoelectric materials σ, κ', and S change with temperature, and in both, generation and refrigeration should be taken into account. However, the simple expression obtained for the efficiency can still be employed with an acceptable degree of accuracy, if approximate averages of values are adopted for these parameters over the temperature range of interest. Appropriate allowances can also be made for contact resistance. Efficiency is clearly a function of the ratio of the load resistance to the sum of the generator arm resistances, and at maximum power output it can be shown that;

$$\eta_P = \frac{T_H - T_C}{\frac{3T_H}{2} + \frac{T_C}{2} + \frac{4}{Z_C}} \tag{2.19}$$

while the maximum efficiency

$$\eta_{max} = \eta_C \gamma \tag{2.20}$$

where

$$\eta_c = \frac{T_H - T_C}{T_H} \tag{2.21}$$

$$\gamma = \frac{\sqrt{1 + Z_C \overline{T}} - 1}{\sqrt{1 + Z_C \overline{T}} + \dfrac{T_C}{T_H}} \tag{2.22}$$

Z_C (the Figure of Merit of the couple) $= \dfrac{S_{ab}^2}{R\kappa'}$ (2.23)

The maximum efficiency is thus the product of the Carnot efficiency, which is clearly less than unity, and γ, which embodies the parameters of the materials. If the geometries of a and b are matched to minimize heat absorption, then;

$$Z_C = \frac{S_{ab}^2}{\sqrt{\kappa_a / \sigma_a} + \sqrt{\kappa_b / \sigma_b})} \tag{2.24}$$

In practice, the two arms of the junction have similar material constants, in which case the concept of a Figure of Merit for a material is employed and given by;

$$Z = \frac{S^2 \sigma}{\kappa} \tag{2.25}$$

where $S^2 \sigma$ is referred to as the electrical power factor.

THERMOELECTRIC MATERIALS

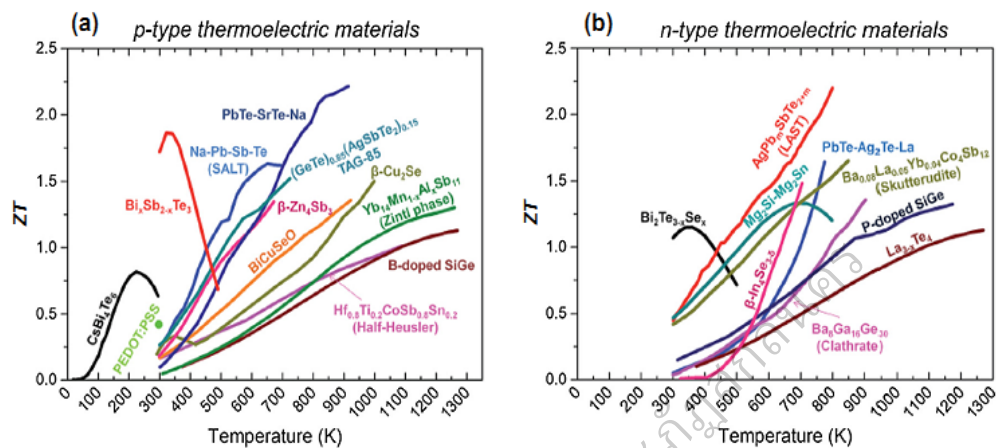## State-of-the-art materials

Figure 8 Summary of the temperature dependence of ZT of thermoelectric n− and p−type materials. Reprinted with permission from Rull−Bravo et al. (Rull−Bravo et al., 2015, pp. 41653−41667)

Currently one of the most popular TE materials that are available on the marked are the tellurides base. Those alloys are good at low temperatures (<523 K, ZT≈ 1.1) when composed of PbTe and TAG−85 materials for medium−range temperatures (523 K to 923 K). In high temperature applications, meaning above 923 K, SiGe alloys are most used, both as n− and p−type materials. Unfortunately these materials exhibit relatively low ZT as illustrated in Figure 8.

The largest ZT have been achieved with chalcogenites and skutterudites but their stability at high temperatures and under oxidizing conditions is poor and the toxicity if those compounds are a major issue (Molinar et al., 2015). Those problems are general issues for current state−of−the art materials hence the great interest in thermoelectric oxides.

CaMnO$_3$

CaMnO$_3$ is a perovskite-type structure with the general formula of ABO$_3$, where A is a rare-earth or alkaline-earth metal and B is a transition metal. The cationic size of A is larger than that of B. The ideal cubic symmetry structure has the B cation in 6-fold coordination, surrounded by an octahedron of anions O^{2-}, and the A cation in 12-fold cuboctahedral coordination. In the idealized cubic unit cell of such a compound (Figure 9), the large A (Ca) cation sits at cube corner positions (0, 0, 0), the small B (Mn) cation sits at body center position (1/2, 1/2, 1/2) and the oxygen anions sit at face centered positions (1/2, 1/2, 0). The relative ion size requirements for stability of the cubic structure are quite stringent, so slight buckling and distortion can produce several low-symmetry distorted versions, in which the coordination numbers of A cations, B cations or both are reduced.

Crystal structure and symmetry can be affected by oxygen and cation stoichiometry. The ideal cubic structure of CaMnO$_3$ can be distorted by octahedral rotation and tilting [96] induced by cation size mismatch and Jahn-Teller effect. Substitution of Ca or Mn with higher valence cations causes the addition of electrons in eg orbitals which causes Jahn-Tellar instability. Moreover, oxygen vacancy can also generate additional electrons in eg orbitals. The generated larger ionic radius of Mn^{3+} (0.645Å) cation in the Mn^{4+} (0.53 Å) matrix, can causes the distortion of the structure. The distorted structures are frequently orthorhombic. The main effects of the various substitutions are to vary the number of electrons in the 3d band and to alter the interatomic distances and bond angles (Coey, Viret, & Von Molnar, 2009). The exchange of electrons between Mn^{3+} and Mn^{4+} takes place via O^{2-} ion with the configuration of Mn^{3+}-O^{2-}-Mn^{4+} and Mn^{4+}-O^2-Mn^{3+}. The configurations, which have partly filled d electrons, are degenerate if the spins of the two d shells are parallel and cause a tendency towards metallic conduction (Kabir et al., 2015). If the manganese spins are not parallel or the Mn-O-Mn bond is bent, the electron transfer becomes more difficult and the mobility decreases. A high symmetry crystal structure and the materials with small electronegativity difference among the constituent elements are

favorable as TEs. The crystal structure with high symmetry provides high band degeneracy and the small electronegativity difference will help to minimize the scattering of charge carriers that consequently increase the mobility of the charge carriers.
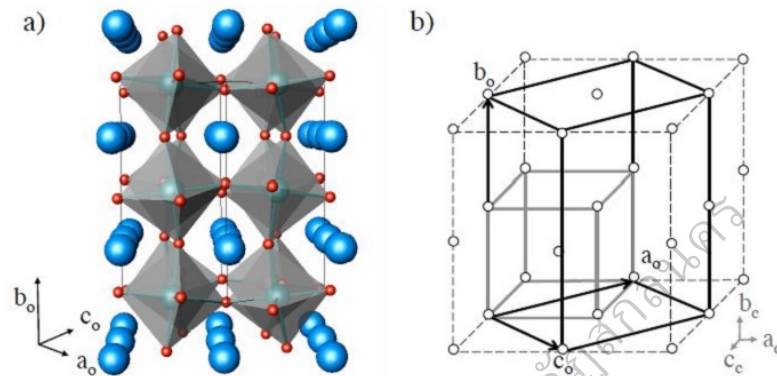

Figure 9 Schematic representations of a) an orthorhombic crystal structure and b) an orthorhombic unit cell (black lines) derived from a pseudo-cubic one (grey lines). Blue spheres correspond to A-sites, green spheres to B-sites, and red spheres to oxygen (Bocher et al., 2008)

Recently, manganite perovskites have been attracted much attention for their interesting electrical and magnetic properties. Among manganite perovskites, $CaMnO_3$ is a good candidate for n-type oxide TE materials due to its high Seebeck co-efficient ($S>300$ μV K^{-1}) at room temperature (Wang et al., 2009; Kabir et al., 2015). However, the TE figure of merit at high temperature remains low due to its large electrical resistivity which exhibits the value of approximately 0.3 Ω cm at room temperature. In general, research into this material is focused on the reduction in electrical resistivity without adversely affecting S or κ. It is found that the electrical resistivity can be decreased by substituting Ca and/Mn with higher valence cations. These cationic substitutions also help to reduce the thermal conductivity of $CaMnO_3$ and resultantly improve the dimensionless figure of merit ZT. Mainly doping for

improvement ZT of $CaMnO_3$ were using 3 method are Ca site doping, Mn site doping and dual doping. Firstly, Rare-earth (Re^{3+}) doped manganite perovskites system with the general formula $Ca_{1-x}Re_xMnO_3$ (Re-rare earth ion) has been suggested as a potential n-type thermoelectric materials (Wang et al., 2009; Lemonnier et al., 2010). It has been found that the doping at Ca site in $CaMnO_3$ causes a decreasing of electrical resistivity (ρ) by increasing electron concentration. On the other hand, doping with a heavy and small Re^{3+} decreased the lattice component of the thermal conductivity (κ_l) and thus gives a good TE performance at high temperature. Due to the large mass difference between the Re^{3+} and Ca^{2+}, Re^{3+} ions can vibrate independently from the other ions and can cause a large local vibration which in turn shortens the phonon mean free path. The decrease of the Mn-O-Mn bond angles can also decrease the κ in a lesser extent. Substituting Ca site with a trivalent cation induces Mn^{3+} cation on the Mn^{4+} matrix, whose ionic radius is larger than that of Mn^{4+} (0.645 and 0.53 Å, respectively) leading to the distortion of the structure. It has been found that this structural distortion is useful to reduce κ (Wang et al., 2013). Secondly, It has also been found that substitution of Mn with other higher valence transition element (e.g. Ta^{5+}, Nb^{5+}, Ru^{5+}) improves the electrical conductivity (Xu et al., 2004; Zhou et al., 2003). The TE properties of $CaMnO_3$, at high temperature, are enhanced by Nb substitution in Mn site and the reported highest ZT value of ~0.32 at 1060 K was achieved for $CaMn_{0.98}Nb_{0.02}O_3$ which is due to its moderately high σ, large S and low κ. The larger ionic radii of both cations Nb^{5+} and Mn^{3+}, generated in the Mn^{4+} matrix causes the structural distortion which is believed to reduce κ (Bocher et al., 2008). Moreover, a microstructure with twinned domains decreases the κ without deteriorating the electronic transport property at high temperature. It is also reported that substitution of Mn with hexavalent transition element such as tungsten

helps to increase the σ and decrease the κ as well. Finally, in the single doped $CaMnO_3$ system, it is found that doping in Ca site with heavy rare-earth elements effectively reduce the κ. On the other hand, doping in Mn-site with other higher valence transition elements effectively increase the σ. Therefore, research has been focused on the simultaneous doping in both Ca and Mn-site to improve TE performance. Some studies show that dual doping using both sites is more effective to improve thermoelectric properties (Kabir et al., 2014; Zhu et al., 2014). However, there are cases where single doping is more effective, such as with Dy and Nb (Muguerra et al., 2011). It is found that dual doping in only Ca-site is more effective than the dual doping using both Ca and Mn site with respect to improving TE properties. Moreover, the appropriate selection of dual doping elements along with appropriate concentration is an effective means for improving TE performance.
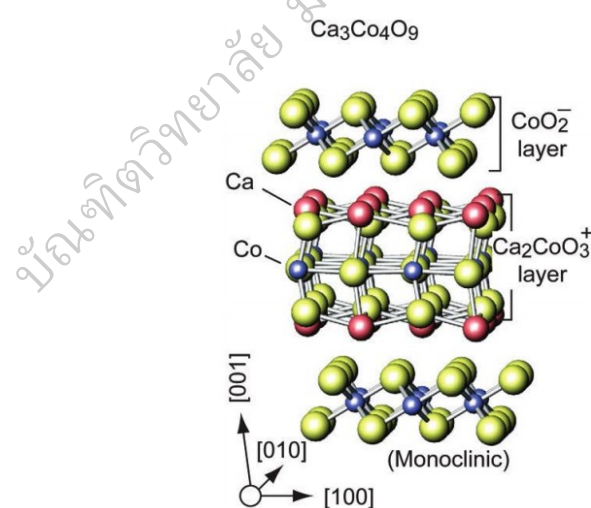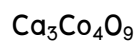
$Ca_3Co_4O_9$

Figure 10. Schematic illustrations of layered cobalt based oxide structures CoO_2 layers consisting of edge-shared CoO_6 octahedral exist $Ca_3Co_4O_9$ (Ohta, H., Sugiura, K., & Koumoto, K., 2008)

Ca$_3$Co$_4$O$_9$ possesses a misfit-layered structure with a CdI$_2$-type hexagonal CoO$_2$ subsystem and a rock salt-type Ca$_2$CoO$_3$ subsystem that are alternately stacked along the c-axis with identical a, c and β parameters but different and incommensurate b parameters. Therefore, this misfit-layered oxide can be described as [Ca$_2$CoO$_3$][CoO$_2$]$_{(b1/b2)}$ with a b1 to b2 ratio of approximately 1.62, where b1 to b2 are two lattice parameters for the rock salt and CoO$_2$ subsystems respectively (Masset et al., 2000; Miyazaki et al., 2002). Shikano et al. have reported a p-type single-crystalline Ca$_3$Co$_4$O$_9$ with a ZT value of 0.83 at 800 (Shikano & Funahashi, 2003, pp. 1851-1853).

The methods to produce polycrystalline Ca$_3$Co$_4$O$_9$ are versatile and are commonly implemented due to the difficulty in single-crystalline sample preparation. Different Ca$_3$Co$_4$O$_9$ syntheses and consolidation processes result in the inferences on the consequent texturing and densification, further affecting the TE properties. Wu et al. reported that highly dense polycrystalline Ca$_3$Co$_4$O$_9$ can be obtained via a spark plasma sintering (SPS) processing (Wu et al., 2013, pp. 2134-2142). With proper SPS conditions, the electrical conductivity may be enhanced. Due to the layered nature of the crystal structure, it is important to take into account the inherent anisotropy due to texturing when characterizing the TE properties of polycrystalline samples (Wu et al 2014). Improving the texturing leads to the increase in "in-plane" electrical conductivity and larger power factor, however, the thermal conductivity increases simultaneously since the loss of structural disorder. Particle size is another factor that affects texturing; with the same consolidation process, highly textured Ca$_3$Co$_4$O$_9$ can be obtained by smaller Ca$_3$Co$_4$O$_9$ particles prepared through wet chemical reactions. Other than the TE properties, the consolidation process also exerts influence on the mechanic properties. Nong et al. reported with Lu and Ag substitutions for Ca atom and the existence of Ag as nanoparticle, the electrical conductivity and Seebeck coefficient can be elevated significantly; together with the decreased thermal conductivity, the highest ZT value of 0.6 at about 900 K for polycrystalline Ca$_3$Co$_4$O$_9$ to date has been achieve. Besides, along with the demonstration of the thermal

stability, heavily doped $Ca_3Co_4O_9$ with metallic nanoinclusions has presented the potential for high temperature TE applications (Van Nong, Pryds, Linderoth, Ohtaki, 2011, pp. 2484–2490).

Thermoelectric module

Ideal thermoelectric materials are indispensable to thermoelectric power generation. However, these materials should have not only a high dimensionless thermoelectric figure of merit ZT but also high chemical stability and should not contain harmful elements. During last few years, oxide based materials, such as $Ca_3Co_4O_9$, $NaCo_2O_4$, $CaMnO_3$, $LaNiO_3$, $SrTiO_3$, In_2O_3 and BiCuSeO have attracted lot of attention as thermoelectric material due to the ease of synthesis and low cost. These materials exhibit best thermoelectric performance at high temperatures >923 K. Most oxide based TEG is currently fabricated using $Ca_3Co_4O_9$ or $NaCo_2O_4$–based material as p–type leg and $CaMnO_3$– or $LaNiO_3$–based material as n–type leg. The performance of such TEG is much lower than expected because of several reasons: (i) high quality at oxide/metal contact junctions; (ii) cracking or exfoliation due to the very different CTEs of oxide and metal; and (iii) the difficulty of having both p–type and n–type from the same parent compound. High working temperatures also make the conventional contact materials and fabrication procedures less viable. The first successful oxide TEG was fabricated using $Ca_3Co_4O_9$ as p–type thermoelement and $CaMnO_3$ as n–type thermoelements, which were joined using a copper strip with a mixture of silver paint and 6 wt% oxide powder (Matsubara, et al., 2001, pp. 3627–3629). Ni and Fe–Cr alloy have also been tested as contact materials for $Ca_3Co_4O_9$. Although the Fe–Cr alloy was better than Ni, the reaction between the contact metals and the oxide at working temperature causes an increase of internal resistance. By introducing a buffer layer (consists of mixture of Ni and $SrRuO_3$ powders) in between Ni and $NaCo_2O_4$ helps to reduce the overall electrical resistivity (Arai et al., 2012, p. 1771). In a recent report, an oxide–based TEG was fabricated using p–type $Ca_3Co_4O_9$ and n–type $(ZnO)_7In_2O_3$ legs (Choi, Lee, Lim, & Seo, 2011, pp. 335–339). The thermoelements were

metallized by coating the ends with Ag paste and Ag wire was used as interconnect. The oxide based TEG with 8 p–n couples along with its power generation characteristics (with hot end at 1050 K). In this study authors mentioned that open circuit voltage of the module was 54% of the theoretical value due to loss of voltage at the contacts. In summary although the oxide materials are considered to be environment friendly, they can be easily synthesized, cheap in cost but still hunt for fabrication of efficient TEG is in progress, which depends on the development of the preparation of low Ohmic electrical contacts shown in figure 14.

Application of thermoelectric generators

Thermoelectric generators can help to reduce the adverse effects of global warming by generating the electricity by harvesting waste heat which is by–product of industries, automobile engines and solar power. These freely available sources of waste heat are the main driving force behind the development of commercial TEGs for electricity generation. Several leading automobile manufacturers are developing TEG (having electrical power of 1 kW) for waste heat recovery to improve the fuel economy of their automobiles (Elsheikh et al., 2014, pp. 337–355). Despite of low TEG efficiency, diligent harvesting of waste heat from resources such as automobile exhaust via judicious design and fabrication methods render TEGs as a worthwhile technology for the automobile manufacturers. A TEG with an efficiency of ≈10% could be used to harvest 35–40% of the energy from the exhaust pipe (having average temperature of ≈523 K) to generate useable power that would contribute directly to the operation of the equipped vehicle, which could increase fuel efficiency by up to 16% (Yu., & Chau, 2009, pp. 1506–1512). In a recent study, 1 kW TEG system (based on n– and p–type half Heuslers) is experimentally demonstrated by recovering the exhaust waste heat from an automotive diesel engine. The TEG exhibited an efficiency of ≈2.1% with ΔT of 340 K and exhaust temperature (T_h) 823 K (Zhang et al., 2015, pp. 946–950). In oxide thermoelectric module application was used 140 pairs of oxide legs. Generating power up to 0.15 W was succeeded. This

module shows excellent resistance to repeated heating and cooling in air because of using Ag paste incorporated the oxide powder. A lithium-ion battery in a portable phone can be charged using this module at T_h higher than 723 K. Power generating modules fabricated using oxide thermoelectric materials could facilitate a revolution in small power sources for mobile devices or automobiles and, moreover, enable recovery of waste heat in the form of electrical energy from sources such as factories and incinerators (Funahashi et al., 2006, pp. 1–3).

LITERATURE REVIEWS

This part will be presented about previous work in all part such as improving ZT of n and p TE materials, fabrication thermoelectric module and application TE module. All work very important for this research because of a data used to improved and fabricated thermoelectric module.

Ohtaki (Ohtaki et al., 1995, pp. 105–111) prepared $(Ca_{0.9}M_{0.1})MnO_3$ (M = Y, La, Ce, Sm, In, Sn, Sb, Pb, Bi) by the solid state reaction (SSR) method. They reported that the substitution at the Ca site increased the electrical conductivity, along with a moderate decrease in the absolute value of the Seebeck coefficient. $(Ca_{0.9}Bi_{0.1})MnO_3$ exhibits the largest power factor, 2.8×10^{-4} W m^{-1} K^{-2} at 1000 K^{-1} and shows ZT 0.085 at 1173 K.

Wang (Wang et al., 2009, pp. 4653–4660) prepared $Ca_{1-x}R_xMnO_3$ (x=0–0.2, R=La, Ce, Pr, Nd, Sm, Eu, Gd, Tb, Dy, Ho, Er, Yb, and Y) ceramics by conventional solid-state reaction method. They reported that the substitution at the Ca site decreased the electrical resistivity and thermal conductivity. $Ca_{0.9}Dy_{0.1}MnO_3$ and $Ca_{0.9}Yb_{0.1}MnO_3$ samples exhibits the largest ZT 0.2 at 1000 K.

Lemonnier (Lemonnier et al., 2010, pp. 887–891) prepared $Ca_{3.95}RE_{0.05}Mn_3O_{10}$ (RE = Ce, Nd, Sm, Eu, Gd, Dy) by the SSR method. They reported that the electron concentration increased with substitute RE^{3+}. In addition, the electrical resistivity and Seebeck coefficient decreased and exhibited metallic behavior. The thermal conductivity of RE = Ce and Dy was lower than RE = Nd, Sm, Eu, and Gd at room temperature. The $ZTx10^{-3}$ value of RE = Ce, Nd, Sm, Eu, Gd, and Dy are 3.91, 4.09, 4.94, 5.83, 2.64, and 5.38, respectively at room temperature.

Huang (Huang et al., 2011, pp. 132–136) synthesized $Ca_{1-x}Bi_xMn_{1-y}V_yO_{3-\delta}$ ($0 \le x = y \le 0.08$) by SSR method. They reported the electrical resistivity decreased due to the increase of carrier concentration. A maximum ZT value reaches to 0.21 for electron–doped $Ca_{0.96}Bi_{0.04}Mn_{0.96}V_{0.04}O_{3-\delta}$ at 1050 K, which is about twice as high as that of $CaMnO_{3-\delta}$. The thermal shock resistance at temperatures between 20 and 450 °C is also highly improved.

Zhang (Zhang et al., 2011, pp. 4171–4175) calculated the electronic structure of $Ca_{0.875}M_{0.125}MnO_3$ (M = Na, Ga) by DFT. They reported that the calculated energy band structure exhibits metallic characteristics shown in Figure 11. The Debye temperature and phonon sound velocity also increased due to Na– and Ga–doped, respectively. The calculated phonon thermal conductivity exhibited was greater for Na–doped than Ga–doped. The Seebeck coefficient also appeared more enhanced with Na–doped as opposed to Ga–doped.
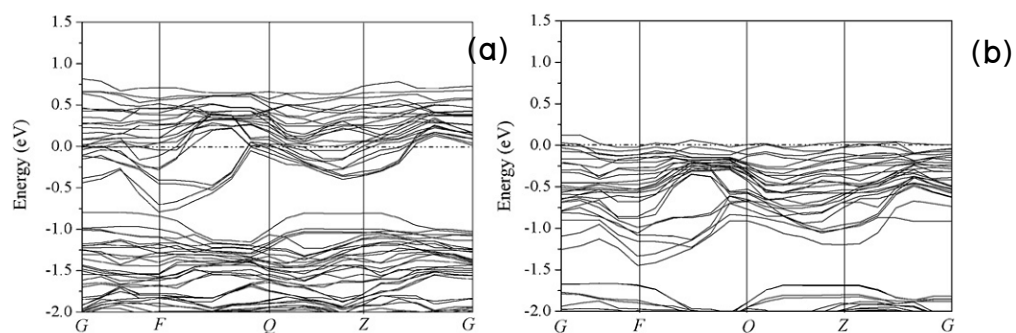

Figure 11 Energy band structure of (a) $Ca_{0.875}Na_{0.125}MnO_3$ and (b) $Ca_{0.875}Ga_{0.125}MnO_3$

Zhu (Zhu et al., 2014, pp. 385–389) synthesized $Ca_{1-2x}Dy_xBi_xMnO_3$ (x = 0.02, 0.05, 0.08 and 0.10) by SSR method. They reported that high relative densities 98 % the electrical resistivity decreased with all doping samples. In addition, electrical resistivity and Seebeck coefficient decrease with increasing Dy and Bi content. Thermal conductivity increases with doping, increasing up to x = 0.08. The highest power factor of 420 $10^{-6}Wm^{-1}K^{-2}$ is obtained at x = 0.02, resulting in the highest dimensionless figure of merit (ZT) of 0.21 at 973 K. This value is four times as much as that of un–doped $CaMnO_3$ ceramics.

Zhu (Zhu et al., 2015, pp. 1535–1539) synthesized $Ca_{1-2x}Dy_xYb_xMnO_3$ (0≤x≤0.10) by SSR method. They reported that high relative densities the electrical resistivity decreased with all doping samples. In addition, the electrical resistivity exhibited semiconductor behavior. The Seebeck coefficients are negative, indicating n–type conduction, and the largest value is obtained –181 µV/K at x=0.02. The highest power factor 415 $10^{-6}Wm^{-1}K^{-2}$) and the highest figure of merit 0.27 are both obtained for x=0.02 sample, and the ZT is about five times as much as un–doped $CaMnO_3$ sample.

Kabir (Kabir et al., 2015, pp. 347–351) prepared $Ca_{1-x}Bi_xMnO_3$ (x = 0, 0.02, 0.03, 0.04, 0.06 and 0.10) by SSR method. They reported that the electrical resistivity and the absolute value of the Seebeck coefficient decrease with increasing Bi doping level; this behavior is indicative an increase in carrier concentration with Bi content. The maximum power factor (4.67 x $10^{-4}Wm^{-1}K^{-2}$) was achieved at 423 K for $Ca_{0.97}Bi_{0.03}MnO_3$ which is four times larger than that of the un–doped $CaMnO_3$. The lowest thermal conductivity (1.4 $Wm^{-1}K^{-1}$) was obtained at 973 K for the same composition (x = 0.03). The maximum ZT value obtained was 0.25 at 973 K for x = 0.03; a threefold increase over that of un–doped $CaMnO_3$.

Xiang (Xiang et al., 2008, pp. 364–369) prepard $Ca_3Co_4O_9/Ag$ thermoelectric composites were fabricated by hot–pressing the composite powders prepared by a solution chemical process. They reported that addition of Ag particles has a strong influence on densification and texture development in $Ca_3Co_4O_9/Ag$

composites. By adding Ag particles, the Seebeck coefficient and electrical resistivity of composites decrease simultaneously. The power factor of $Ca_3Co_4O_9/Ag$ is found to be improved due to the remarkable reduction in resistivity. However, the value decreases when the Ag content is above 7.5 vol.% because the value of S is obviously deteriorated by the presence of large amounts of Ag particles.

Wang (Wang et al., 2009, pp. 817–821) prepared high–textured Ag–doped or/and Ag–added $Ca_3Co_4O_9$ ceramic specimens have been prepared by a cold–pressing technique. They reported that the substitution of Ag^+ for Ca^{2+} causes the reduction of resistivity and the enhancement of thermoelectric power simultaneously, whereas the addition of metal Ag results in the decrease on resistivity together with thermoelectric power. Both Ag^+ doping and Ag addition can enhance power factor; however, the doping of Ag^+ is advantageous for the suppression of thermal conductivity whereas the addition of Ag facilitates thermal conductivity. $Ca_{2.7}Ag_{0.3}Co_4O_9/Ag$–10wt% composite exhibits a quite respectable thermoelectric performance; the dimensionless figure of merit ZT can reach 0.5 at 1000K.

Constantinescu (Constantinescu et al., 2013, pp. 511–515) prepared $Ca_{3-x}Sr_xCo_4O_9$ with x = 0.00, 0.01, 0.03, 0.05, 0.07, and 0.10, by SSR method. They reported that the electrical resistivity decreases and Seebeck coefficient slightly raises when Sr content increases until 0.07 Sr addition. The maximum power factor which is maximum for the 0.07 Sr–doped samples with values around 0.12 and 0.30 $10^{-3}Wm^{-1}K^{-2}$, respectively, which are about 30% and 50% higher than the obtained for the un–doped samples at room temperature to 1073 K.

Wu (Wu et al., 2013, pp. 511–515) prepared dual doping Y and Fe $Ca_{3-x}Y_xCo_{4-y}Fe_yO_{9+}\delta$ (0 ≤ x ≤ 0.3, 0 ≤ y ≤ 0.1) by auto–combustion reaction and followed by a spark plasma sintering (SPS) method. They reported that the Fe substitution at the Co–sites effectively reduces the electrical resistivity in the high temperature region, while the Seebeck coefficient is influenced only slightly. Y substitution for Ca^{2+} leads to an increase in the Seebeck coefficient but also in the electrical resistivity. With proper additional Fe doping, the rising q was compensated,

together with the improved Seebeck coefficient leading to an improvement of the PF. The $Ca_{2.9}Y_{0.1}Co_{3.97}Fe_{0.03}O_{9+}$ δ sample exhibited maximum power factor reaches a value of 510 $10^{-6}Wm^{-1}K^{-2}$ and ZT 0.22 at 1073 K which is about 18% higher than that of un-doped Co349.

Tian (Tian et al., 2014, pp. 311-315) prepared co-doping Bi and Fe $Ca_{3-x}Bi_xCo_{4-y}Fe_yO_{9+}$ δ (x =0, y =0; x = 0.3, y =0; x = 0.3, y = 0.1) by SSR and followed by a spark plasma sintering (SPS) method. They reported that Bi substitution leads up to 40% reduction in the thermal conductivity, which is mainly associated with doping-induced point defect phonon scattering. In addition, the power factor was found to be increased by ≈33% by the co-doping of Fe and Bi. In present study, the thermoelectric figure of merit achieves ≈0.4 at 973 K by the co-doped sample $Ca_{2.7}Bi_{0.3}Co_{3.9}Fe_{0.1}O_{9+}$ δ.

Cho (Cho et al., 2015, pp. 3621-3626) prepared $Ca_{3-x}Bi_xCo_4O_9$ (x =0, 0.025, 0.05, 0.1, 0.15, 0.2) by SSR method. They reported that the Seebeck coefficient increased with increasing Bi content due to the decrease in the hole carrier concentration after Bi doping. As the amount of Bi was increased, the electrical resistivity initially decreased but then increased with further addition of Bi.

Lin (Lin et al., 2016, pp. 44-49) prepared $Ca_3Co_4O_9$ small amounts of silver nanoparticles (AgNPs) by SSR and followed by a spark plasma sintering (SPS) method. They reported that achieve a lower thermal conductivity due to the increased phonon scattering, decreasing from 3.1 $Wm^{-1}K^{-1}$($Ca_3Co_4O_9$) to 1.6 $Wm^{-1}K^{-1}$ (AgNPs/ $Ca_3Co_4O_9$) at 700 K. Besides, the nano-sized AgNPs effectively strengthen the p-type $Ca_3Co_4O_9$ grain orientation (from 0.5 to 0.7), leading to a significant enhancement of the electrical conductivity. As a result, the $Ca_3Co_4O_9$ sample containing 2.0 vol% AgNPs exhibits an exceedingly enhanced ZT value ≈0.1 at 700 K, which is about 5 times higher than that of pure bulk $Ca_3Co_4O_9$.

Funahashi (Funahashi et al., 2004, pp. 1036–1038) fabricated thermoelectric unicouple composed of p–type $Ca_{2.7}Bi_{0.3}Co_4O_9$ (Co–349) and n–type $La_{0.9}Bi_{0.1}NiO_3$ (Ni–113) bulks were constructed using Ag paste containing p– and n–type oxide powders, prepared from the same bulks, for connection of the p and n legs, respectively. Internal resistance (R_I) of the unicouple corrected using Ag paste containing 6 wt. % of the oxide powders is 26.2 mV at 1073 K in air and decreases with increasing temperature. Maximum output power (P_{max}), evaluated using the formula $P_{max} = V_o^2 / 4R_I$, (V_O is open–circuit voltage), is 94 mW at 1073 K (ΔT=500 K) and increases with temperature. This value corresponds to a volume power density of 0.66 W/cm^3.
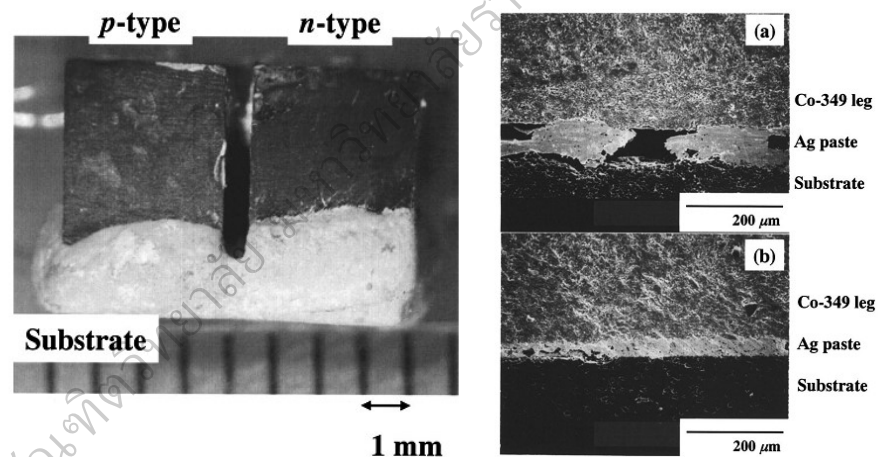

Figure 12 Image of a thermoelectric unicouple composed of p–type Co–349 and n–type Ni–113 oxide materials (left) and scanning electron microscopic images at p–leg/Ag junctions containing (a) 0 and (b) 6 wt.% of Co–349 powder after the heating–cooling cycle (right)

Funahashi (Funahashi et al., 2006, pp. 1–3) fabricated thermoelectric module 140 pairs composed of p–type $Ca_{2.7}Bi_{0.3}Co_4O_9$ (Co–349) and n–type $La_{0.9}Bi_{0.1}NiO_3$ (Ni–113) bulks were constructed using Ag paste. The module's open circuit voltage increases with increasing hot–side temperature (T_H) and reaches 4.5 V at a T_H of 1072 K in air. No deterioration in output power was seen when power generation was carried out ten times at a T_H of 723 K with intermediate cooling to room temperature internal resistance (R_i) of module ≈ 1 ohm.
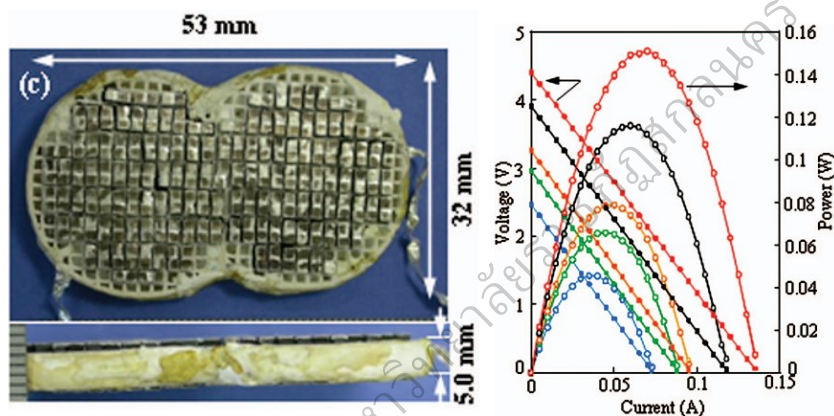

Figure 13 Image of a thermoelectric 140 pair composed of p–type Co–349 and
n –type Ni–113 oxide materials (left) and thermoelectric generation characteristics of the oxide
module (right)

Choi (Choi et al., 2011, pp. 335–339) fabricated thermoelectric module 44 pairs composed of p–type $Ca_3Co_4O_9$ and n–type $(ZnO)_7In_2O_3$ legs were constructed using Ag paste. The maximum power obtained was 423 mW, under the thermal condition of a hot–side temperature of 1100 K and a temperature difference $\Delta T = 673$ K. The thermoelectric figure of merit values of the p–type and n–type legs at 1100 K were $0.55 \times 10^{-4} K^{-1}$ and $1.35 \times 10^{-4} K^{-1}$, respectively.
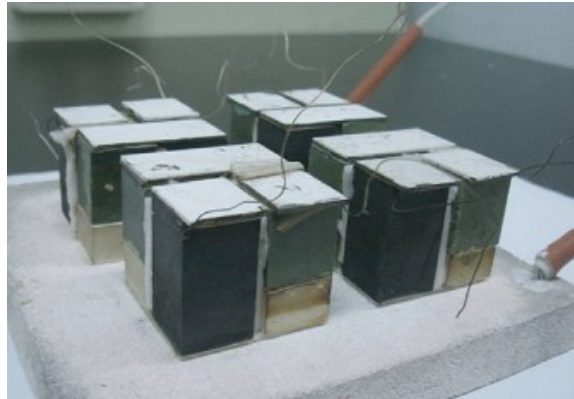
Figure 14 Photograph of the oxide thermoelectric module for power generation measurements with eight p–n couples, taken after several power generation measurements

Park (Park and Lee, 2013, pp. 335–339) fabricated thermoelectric modules of $\prod$–shaped 1–, 2–, and 4–pairs composed of p–type $Ca_{2.76}Cu_{0.24}Co_4O_9$ and n–type $Ca_{0.8}Dy_{0.2}MnO_3$ oxide materials were constructed using Ag paste. The output powers of –, 2–, and 4–pairs increase with an increase in temperature difference ∆T between the hot– and cold–side temperatures of the modules show in Figure 15 (right).
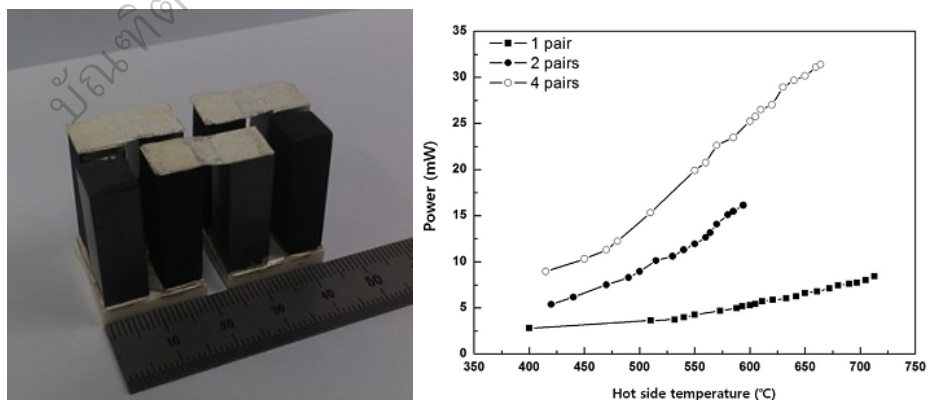

Figure 15 Photographs of four–pair $\prod$–shaped thermoelectric modules with Ag electrode (left) and maximum output powers of 1–, 2–, and 4–pair modules as a function of hot–side temperature (right)

Goudarzi (Goudarzi et al., 20013, pp. 2127–2133) constructed thermoelectric generator system by using commercial 21 module size of 56 mm x 56 mm for produce electricity from wood stove. The maximum output power 14.7 W at ΔT 452 K (T_h= 773 K) to fulfill the basic needs of domestic electricity, hot water, and essential heat for warming the room and cooking.

Figure 16 Water cooling system and integration thermoelectric module on wood stove

O'Shaughnessy (O'Shaughnessy et al., 20013, pp. 374–385) developed a prototype electrical generator for portable stoves commonly in use in the developing world. They reported that a single thermoelectric module is utilized to convert a small portion of heat from the stove to electricity. The electricity produced is used to charge a single 3.3 V lithium–iron phosphate battery and drive a low power fan, as well as some other auxiliary features. A maximum TEG power output of 5.9 W has been obtained. On average, 3 W h of energy was stored in a battery during a typical 1 h long burn. Three 1 h long burns produced sufficient energy to fully charge the battery.
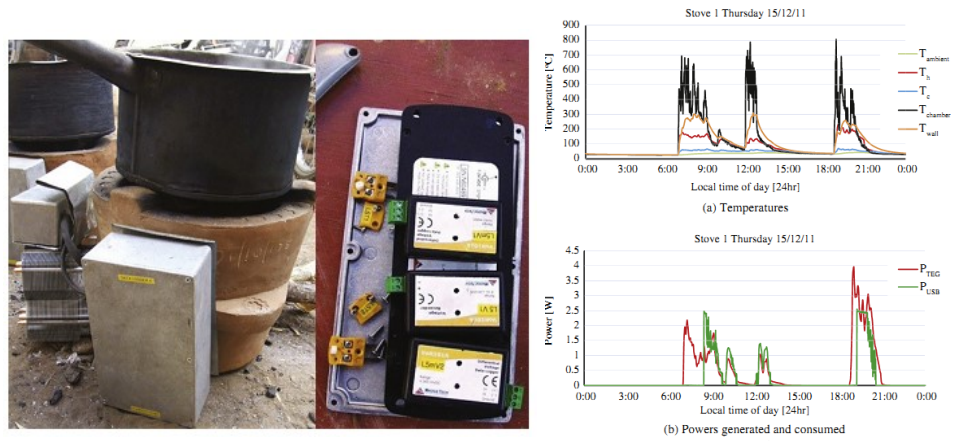
Figure 17 The prototype stoves (left) and power generation depend

temperature (right)